Measurement and analysis of the ^241 Am(n,γ) cross section with liquid scintillator detectors using time-of-flight spectroscopy at the n_TOF facility at CERN

(n_TOF Collaboration) Fraval, K.; Gunsing, F.; Altstadt, S.; Andrzejewski, J.; Audouin, L.; Barbagallo, M.; Bécares, V.; Bečvář, F.; Belloni, F.; Berthoumieux, E.; ...

Source / Izvornik: **Physical Review C - Nuclear Physics, 2014, 89**

Journal article, Published version
Rad u časopisu, Objavljena verzija rada (izdavačev PDF)

https://doi.org/10.1103/PhysRevC.89.044609

Permanent link / Trajna poveznica: https://urn.nsk.hr/urn:nbn:hr:217:713219

Measurement and analysis of the ^{241}Am(n,γ) cross section with liquid scintillator detectors using time-of-flight spectroscopy at the n_TOF facility at CERN

K. Fraval,[1] F. Gunsing,[1,*] S. Altstadt,[2] J. Andrzejewski,[3] L. Audouin,[4] M. Barbagallo,[5] V. Bécares,[6] F. Bečvář,[7] F. Belloni,[1] E. Berthoumieux,[1,8] J. Billowes,[9] V. Boccone,[8] D. Bosnar,[10] M. Brugger,[8] M. Calviani,[8] F. Calviño,[11] D. Cano-Ott,[6] C. Carrapiço,[12] F. Cerutti,[8] E. Chiaveri,[1,8] M. Chin,[8] N. Colonna,[5] G. Cortés,[11] M. A. Cortés-Giraldo,[13] M. Diakaki,[14] C. Domingo-Pardo,[15] I. Duran,[16] R. Dressler,[17] N. Dzysiuk,[18] C. Eleftheriadis,[19] A. Ferrari,[8] S. Ganesan,[20] A. R. García,[6] G. Giubrone,[15] M. B. Gómez-Hornillos,[11] I. F. Gonçalves,[12] E. González-Romero,[6] E. Griesmayer,[21] C. Guerrero,[8] P. Gurusamy,[20] A. Hernández-Prieto,[8,11] D. G. Jenkins,[22] E. Jericha,[21] Y. Kadi,[8] F. Käppeler,[23] D. Karadimos,[14] N. Kivel,[17] P. Koehler,[24] M. Kokkoris,[14] M. Krtička,[7] J. Kroll,[7] C. Lampoudis,[1] C. Langer,[2] E. Leal-Cidoncha,[16] C. Lederer,[2,25] H. Leeb,[21] L. S. Leong,[4] R. Losito,[8] A. Mallick,[20] A. Manousos,[19] J. Marganiec,[3] T. Martínez,[6] C. Massimi,[26] P. F. Mastinu,[18] M. Mastromarco,[5] M. Meaze,[5] E. Mendoza,[6] A. Mengoni,[27] P. M. Milazzo,[28] F. Mingrone,[26] M. Mirea,[29] W. Mondalaers,[30] C. Paradela,[16] A. Pavlik,[25] J. Perkowski,[3] A. Plompen,[30] J. Praena,[13] J. M. Quesada,[13] T. Rauscher,[31] R. Reifarth,[2] A. Riego,[11] M. S. Robles,[16] F. Roman,[8,29] C. Rubbia,[8,32] M. Sabaté-Gilarte,[13] R. Sarmento,[12] A. Saxena,[20] P. Schillebeeckx,[30] S. Schmidt,[2] D. Schumann,[17] G. Tagliente,[5] J. L. Tain,[15] D. Tarrío,[16] L. Tassan-Got,[4] A. Tsinganis,[8] S. Valenta,[7] G. Vannini,[26] V. Variale,[5] P. Vaz,[12] A. Ventura,[27] R. Versaci,[8] M. J. Vermeulen,[22] V. Vlachoudis,[8] R. Vlastou,[14] A. Wallner,[25] T. Ware,[9] M. Weigand,[2] C. Weiß,[21] T. Wright,[9] and P. Žugec[10]

(n_TOF Collaboration)[†]

[1]*CEA Saclay - Irfu, Gif-sur-Yvette, France*

[2]*Johann-Wolfgang-Goethe Universität, Frankfurt, Germany*

[3]*Uniwersytet Łódzki, Lodz, Poland*

[4]*Centre National de la Recherche Scientifique/IN2P3 - IPN, Orsay, France*

[5]*Istituto Nazionale di Fisica Nucleare, Bari, Italy*

[6]*Centro de Investigaciones Energeticas Medioambientales y Tecnológicas (CIEMAT), Madrid, Spain*

[7]*Charles University, Prague, Czech Republic*

[8]*European Organization for Nuclear Research (CERN), Geneva, Switzerland*

[9]*University of Manchester, Oxford Road, Manchester, United Kingdom*

[10]*Department of Physics, Faculty of Science, University of Zagreb, Croatia*

[11]*Universitat Politecnica de Catalunya, Barcelona, Spain*

[12]*Instituto Tecnológico e Nuclear, Instituto Superior Técnico, Universidade Técnica de Lisboa, Lisboa, Portugal*

[13]*Universidad de Sevilla, Spain*

[14]*National Technical University of Athens (NTUA), Greece*

[15]*Instituto de Física Corpuscular, CSIC-Universidad de Valencia, Spain*

[16]*Universidade de Santiago de Compostela, Spain*

[17]*Paul Scherrer Institut, Villigen PSI, Switzerland*

[18]*Istituto Nazionale di Fisica Nucleare, Laboratori Nazionali di Legnaro, Italy*

[19]*Aristotle University of Thessaloniki, Thessaloniki, Greece*

[20]*Bhabha Atomic Research Centre (BARC), Mumbai, India*

[21]*Atominstitut, Technische Universität Wien, Austria*

[22]*University of York, Heslington, York, United Kingdom*

[23]*Karlsruhe Institute of Technology, Campus Nord, Institut für Kernphysik, Karlsruhe, Germany*

[24]*Department of Physics, University of Oslo, N-0316 Oslo, Norway*

[25]*University of Vienna, Faculty of Physics, Austria*

[26]*Dipartimento di Fisica e Astronomia, Università di Bologna, and Sezione INFN di Bologna, Italy*

[27]*Agenzia nazionale per le nuove tecnologie, l'energia e lo sviluppo economico sostenibile (ENEA), Bologna, Italy*

[28]*Istituto Nazionale di Fisica Nucleare, Trieste, Italy*

[29]*Horia Hulubei National Institute of Physics and Nuclear Engineering - IFIN HH, Bucharest - Magurele, Romania*

[30]*European Commission JRC, Institute for Reference Materials and Measurements, Retieseweg 111, B-2440 Geel, Belgium*

[31]*Department of Physics and Astronomy - University of Basel, Basel, Switzerland*

[32]*Laboratori Nazionali del Gran Sasso dell'INFN, Assergi (AQ), Italy*

(Received 21 November 2013; published 23 April 2014)

The ^{241}Am(n,γ) cross section has been measured at the n_TOF facility at CERN using deuterated benzene liquid scintillators, commonly known as C_6D_6 detectors, and time-of-flight spectrometry. The results in the resolved resonance range bring new constraints to evaluations below 150 eV, and the energy upper limit was extended

*Corresponding author: frank.gunsing@cea.fr

[†]www.cern.ch/ntof

from 150 to 320 eV with a total of 172 new resonances not present in current evaluations. The thermal capture cross section was found to be $\sigma_{th} = 678 \pm 68$ b, which is in good agreement with evaluations and most previous measurements. The capture cross section in the unresolved resonance region was extracted in the remaining energy range up to 150 keV, and found to be larger than current evaluations and previous measurements.

DOI: 10.1103/PhysRevC.89.044609 PACS number(s): 25.40.Lw, 25.40.Ny, 28.20.Fc

INTRODUCTION

Nuclear power using fission technology has to cope with the issue of radioactive waste, mostly coming from irradiated construction materials in the reactor and spent fuel. The latter carries the major disadvantage of having very long-lived and highly radioactive isotopes, consisting of fission products and actinides. For example, the spent fuel of a pressurized water reactor (PWR) using MOX fuel with 8.2% content of Pu, after a burn-up of 43.5 GW·d/t and four years of cooling has a 0.6% mass content of minor actinides, among which is 50% of ^{241}Am. Isotopes of Am and Np are responsible for the totality of the long-term radiotoxicity for times greater than 10^5 years [1–3]. The nucleus ^{241}Am with spin parity $J^\pi = 5/2^-$ has a half life of 432 y, and ^{237}Np a half life of 2.14×10^6 years. Also, a high burn-up of fuel in existing nuclear reactors inevitably leads to the accumulation of more minor actinides. Transmutation or incineration of actinides is a possibility to be considered, either in conventional uranium-plutonium fuel-cycle nuclear reactors [4,5] or in future thorium-uranium based reactors [6].

Experimental nuclear research is needed to bring accurate cross section data on nuclei of interest. This work, as a part of the EC-FP7 ANDES project [7], is concerned with the ^{241}Am(n,γ) reaction, which is on the High Priority List of the Nuclear Energy Agency [8–10]. Current available experimental data on the ^{241}Am neutron cross section include activation and pile oscillation measurements to retrieve the thermal capture cross section, and time-of-flight experiments which allow resonance analysis.

A measurement of the thermal cross section using pile oscillations was performed by Pomerance *et al.* in 1955 [11]. Most thermal data are obtained using the activation technique, including the work of Bak *et al.* [12], Dovbenko *et al.* [13], Harbour *et al.* [14], Gavrilov *et al.* [15], Shinohara *et al.* [16], Maidana *et al.* [17], Fioni *et al.* [4], Nakamura *et al.* [18], Bringer *et al.* [19], Belgya *et al.* [20], and Genreith *et al.* [21]. These data are summarized in Fig. 11.

It should be noted that the activation technique requires the use of the Westcott convention, which assumes a shape for the neutron flux and energy dependence of the cross section. The presence of large resonances at very low energy in ^{241}Am complicates this analysis step, and corrections are needed. This may partly explain the difficulties and discrepancies in the past measurements.

Older time-of-flight measurements are the transmission data sets from Derrien and Lucas [22] and from Kalebin *et al.* [23,24], as well as the capture data from Weston and Todd [25] and from Van Praet *et al.* [26].

More recently two time-of-flight measurements of ^{241}Am have been published. The neutron capture measurement of

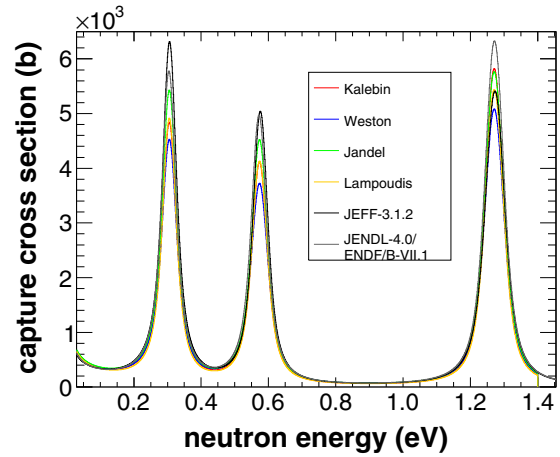

FIG. 1. (Color online) The ^{241}Am(n,γ) cross section at 300 K for the first three resonances for different measurements and evaluations, all calculated from resonance parameters.

Jandel *et al.* [27] was performed in Los Alamos National Laboratory, using the 4π calorimeter of BaF_2 crystals DANCE. The cross section was measured using a 219-μg ^{241}Am target at a 20.2-m distance from the neutron source. The analysis was performed from 0.02 eV to 320 keV, and included resolved resonance shape analysis from 0.02 to 12 eV. The work of Lampoudis *et al.* [28] was performed at the GELINA facility in Geel, Belgium. It used a 325-mg ^{241}Am content and included both transmission and capture measurements. The transmission measurement was performed at a flight path of 26.45 m and the capture experiment at a flight path of 12.5 m, using two liquid scintillator detectors based on deuterated benzene ($C_6\ ^2H_6$), in the following denoted as C_6D_6. A resonance shape analysis was performed up to 110 eV. The capture data were normalized to the transmissions data, expected to give an absolute normalization.

In evaluated data libraries, ENDF/B-VII.1 [29] adopted the resonance parameters evaluated by JENDL-4.0 [30], which took into account the work of Jandel *et al.* [27], whereas the parameters of JEFF-3.1.2 [31] are based on data from Refs. [22,23,25,26,32–36]. Figure 1 shows the discrepancies between experimental and evaluated data sets in the ^{241}Am neutron capture cross section for the first three resonances, of which the parameters are given in Table I.

In order to improve the accuracy on the neutron induced cross sections of ^{241}Am, a new neutron capture measurement has been performed at the neutron time-of-flight facility n_TOF at CERN and is reported in this paper.

I. EXPERIMENTAL SETUP

A. The n_TOF facility

The neutron time-of-flight facility n_TOF is located at CERN (European Organization for Nuclear Research), and uses the 20-GeV/c protons extracted from the Proton Synchrotron (PS) on a 40-cm-thick and 60-cm-diameter lead spallation target. The proton pulses from the PS have an rms width of 7 ns, a nominal intensity of 7×10^{12} protons per pulse, and a minimum repetition rate of 1.2 s, resulting in a very high instantaneous neutron flux. Charged particles created during the spallation process are deflected from of the beam by a dipole magnet with a bending power of 3.63 T m.

The neutrons, moderated by 1 cm of cooling water and 4 cm of borated water, are collimated in a vacuum beam guide leading to the experimental area located 182.3 m away from the spallation target.

The neutron fluence is measured at the entrance of the experimental area by four silicon detectors viewing an in-beam ^{6}Li deposit [37], and two MicroMegas chambers containing ^{10}B and ^{235}U converters [38,39]. The combined use of these detectors allows an accurate measurement of the neutron flux from thermal energy to the GeV region. As for γ detection, the measurements carried out at n_TOF use C_6D_6 liquid scintillators or a 4π total absorption calorimeter (TAC) [40], made of 40 BaF_2 scintillation crystals. This work was performed with two optimized Bicron C_6D_6 detectors. More details on the facility can be found in Refs. [41] and [42].

B. Data acquisition

The data acquisition at n_TOF is based on flash ADCs from Acqiris [43], using a zero suppression technique to lower data transfer rates. For the C_6D_6 detector setup modules with eight-bit amplitude resolution were used at a sampling frequency of 500 MHz. The available memory of 48 MSamples allowed us to store data up to 96 ms, or an equivalent neutron energy of 0.019 eV. However, the neutron flux measurements were performed with less memory, allowing a lowest neutron energy of 26.3 meV. The recorded signals exceeding the detection threshold of 150 keV were fitted to a reference shape in order to extract the amplitude and time of flight, which were stored in DST (data summary tape) files for further analysis.

TABLE I. A comparison of the parameters of the first three resonances at 0.306, 0.573, and 1.271 eV from measurements and evaluations.

Reference	0.306 eV		0.573 eV		1.271 eV	
	$g\Gamma_n$ (meV)	Γ_γ (meV)	$g\Gamma_n$ (meV)	Γ_γ (meV)	$g\Gamma_n$ (meV)	Γ_γ (meV)
Derrien [22]					0.161	46.5
Kalebin [24]	0.0275	45	0.0464	43	0.165	41
Weston [25]	0.027	46.9	0.047	47.3	0.157	49.2
Jandel [27]	0.0311	44.4	0.050	43.3	0.173	45.3
Lampoudis [28]	0.0373	41.55	0.0458	42.11	0.218	41.68
JEFF-3.1.2 [31]	0.0356	43.52	0.055	40.67	0.169	48.44
JENDL-4.0 [30]	0.0329	44.4	0.0558	43.3	0.190	45.3

TABLE II. The composition of the ^{241}Am sample.

Element/isotope (in compound)	Mass (mg)	Density (10^{-4} atoms/b)
Al (Al_2O_3)	159	30.2
O (Al_2O_3)	142	45.3
^{241}Am (AmO_2)	32.2 ± 0.7	0.68 ± 0.02
O (AmO_2)	4.28	1.36
^{237}Np	1.1	0.024
^{240}Pu	0.02	0.00046

C. The ^{241}Am sample

The sample used for this experiment was a solution of americium oxide ($^{241}AmO_2$) in an aluminium oxide (Al_2O_3) matrix, and was part of a batch of samples produced for (n,2n) measurements [44]. After drying and calcination the material was pressed in a cylindrical pellet of 0.342 g and 12.26 mm diameter, with a 32.2 ± 0.7-mg content of ^{241}Am (determined by calorimetry [45]); see Table II. The pellet was encapsulated in an aluminium canning and sealed with Stycast. A schematic view of the definitive sample is shown in Fig. 2. A dummy sample without ^{241}Am was available as well.

The main impurity in the sample is ^{237}Np, originating from the α decay of ^{241}Am. From the analysis of some strong resonances, visible in the spectrum, the amount was estimated to be about 2.4×10^{-6} atoms/b. Also, some ^{240}Pu is present in the sample, as seen in Fig. 9 where the 1.05-eV resonance is clearly visible on the capture yield. Its density was estimated to be about 4.6×10^{-8} atoms/b. Note that this is only an estimation fitted on the 1.05-eV resonance, however it does not contribute enough to the capture yield to extract a precise density. In the end ^{237}Np and ^{240}Pu resonances were included as well in the resonance analysis.

The radioactivity of the sample was about 3 GBq at the time of the measurement, dominated by 60-keV γ rays. The high activity was drawing a very high current C_6D_6 photomultiplier and voltage divider, resulting in random periods of zero output signal lasting for several μs. This was solved by placing 2-mm lead plates in front of each detector to shield them from the

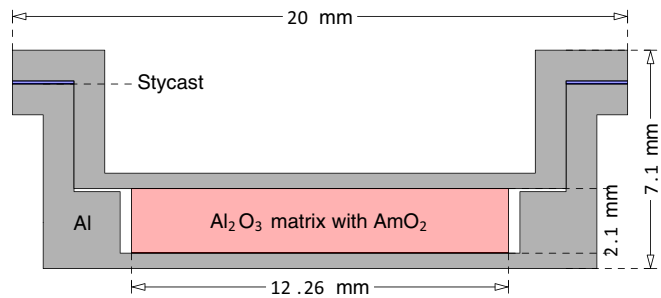

FIG. 2. (Color online) A schematic view of the ^{241}Am sample used in the experiment.

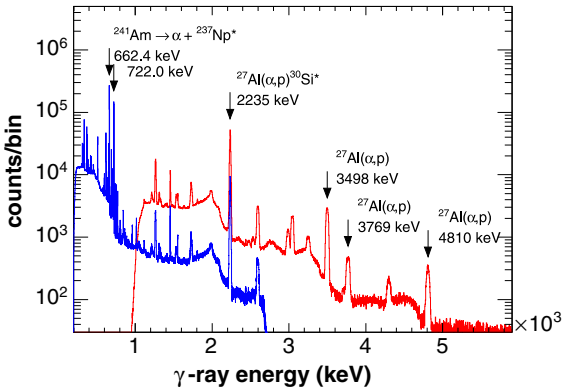

FIG. 3. (Color online) The γ-ray spectrum of the ^{241}Am measured in two energy ranges with a HPGe setup [46]. Some characteristic γ rays from α decay or from α induced reactions are shown as well.

low energy photons and therefore lowering considerably the count rate.

The α activity of the sample generated 2235-keV photons coming from the (α, p) reaction on ^{27}Al in the Al_2O_3 matrix.

The response to these γ rays contributed to the background which is about 90% of the signal at thermal energies. In a separate measurement with HPGe detectors [46] this γ ray is clearly visible, as shown in Fig. 3. This characteristic 2.235-MeV γ-ray transition was used as a reference point for a dynamical energy calibration (see Sec. II A).

D. The C_6D_6 detectors

Two Bicron C_6D_6 liquid scintillator detectors were used for the γ-ray detection. The main advantages of these detectors are a very good time resolution, with pulse widths of the order of 10 ns, and a low sensitivity to scattered neutrons. On the other hand, these detectors have low efficiency and poor energy resolution. Figure 4 shows an MCNP [47] geometry of the sample and detectors implemented for this analysis.

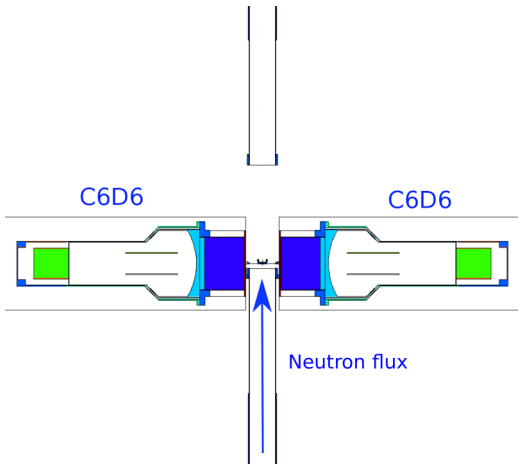

FIG. 4. (Color online) A schematic view of the detector and sample setup used for this experiment. The distance between the two deuterated benzene, C_6D_6, detectors was 6.1 cm.

II. DATA PROCESSING

A. Amplitude-energy calibration

Three standard calibration sources were used for the amplitude to energy calibration: ^{137}Cs providing a 662-keV γ ray, ^{88}Y providing two simultaneous γ rays of 898 and 1836 keV, and an Am-Be source providing a 4.4-MeV γ ray from the (α, n) reaction on ^{9}Be. To obtain the calibration function for each detector an MCNP simulation of the detectors' response was performed, and was adjusted to match the measured response data, with the free parameters being the resolution and calibration functions both chosen as second order polynomials, as applied in Ref. [48]. The measured and simulated response and the resulting calibration are shown in Fig. 5.

However the amplitude response was not stable over time, and a dynamical adjustment was applied using the 2235-keV γ ray from the ^{27}Al$(\alpha, p)^{30}$Si* reaction, which was clearly visible in every measurement run. The procedure was very similar to the one used with the standard calibration sources, the C_6D_6 response to the 2235-keV photon was simulated and fit to the experimental data (see Fig. 5). In practice, the calibration function f was used on a corrected amplitude $k \times A$ in order to give the correct energy $f(k \times A) = E$. The correction factor k was determined by linearly scaling the observed amplitude response of the 2235-keV photon to the amplitude response at the time of the calibration. This gives an average correction factor k of respectively 0.90 and 0.97 for the two detectors, with a standard deviation of 0.04. Figure 6 shows the deposited energy spectra for the Am sample with and without beam (where the 2.235-MeV photon energy deposition is clearly seen), together with the 250-μm-thick gold sample spectrum. The spectra were processed with a software threshold of 300 keV, larger than the threshold of approximately 150 keV of the data acquisition.

B. Weighting function procedure

The pulse height weighting technique (PHWT) was used to determine the efficiency for a capture reaction ϵ_c independent

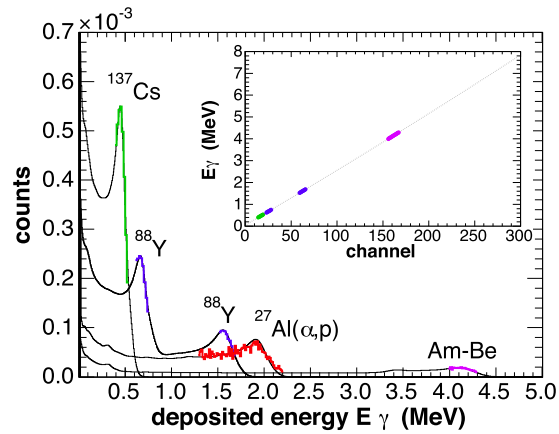

FIG. 5. (Color online) The simulated detector responses and measured spectra from calibration sources. The resulting energy calibration is shown in the inset. The highlighted regions correspond to the intervals where the calibrations sources were fitted.

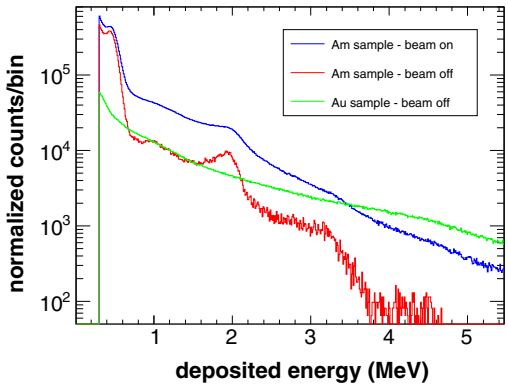

FIG. 6. (Color online) The deposited energy spectra for the Am sample with and without beam, and the gold sample, corresponding to all neutron energies with times of flight between 10^4 and 10^8 ns. The beam-off spectrum is normalized to acquisition time, and the beam-on is normalized to neutrons received relative to the Am sample spectrum.

from the details of the gamma-ray cascade spectrum following neutron capture. This method, explained in more detail in for example [49,50], exploits the low efficiency ϵ_i for one γ ray E_i of the cascade of the total energy $S_n + E_n$, corresponding to the sum of the neutron binding energy S_n and the neutron kinetic energy E_n, such that

$$\epsilon_c(E_n) = 1 - \prod_i (1 - \epsilon_i) \approx \sum_i \epsilon_i. \quad (1)$$

The main difficulty resides in the random character of the γ cascade, since many de-excitation paths to the ground state are possible, resulting in many different values for the total efficiency $\epsilon_c(E_n)$. The idea to circumvent this issue is to use a weighting function $W(E)$ in order to make the efficiencies ϵ_i proportional to the γ energy E_i by modifying the detector response function $R_i(E)$ so that the γ-ray efficiency $\epsilon_i = \int R_i(E)dE$ becomes proportional to its energy

$$\epsilon_i = \int_{E_{\rm low}}^{E_{\rm up}} W(E)R_i(E)dE = k \times E_i, \quad (2)$$

and therefore the cascade efficiency

$$\epsilon_c(E_n) \approx \sum_i \epsilon_i = \sum_i E_i = S_n + E_n, \quad (3)$$

when the proportionality constant k is set to 1 per energy unit. The weighting function $W(E)$ was taken as a fourth order polynomial $\sum_0^4 a_i E^i$ of which the coefficients a_i were determined by likelihood maximization using simulated detector response functions to several monoenergetic γ rays. The detailed geometry in these simulations includes the sample, canning, detectors, and immediate surroundings as shown in Fig. 4. The effective threshold used for event selection was taken as the lower limit $E_{\rm low}$ in Eq. (2), while the upper limit $E_{\rm up}$ was chosen slightly above the excitation energy $S_n + E_n$. The possible influence of the difference between the Am and Au γ spectra under the threshold on the normalization is discussed in Sec. III C.

C. Deadtime correction

From the time distribution between consecutive events in the same detector, a deadtime of approximately $\tau = 25$ ns was observed. Therefore in the analysis a slightly higher deadtime of $\tau = 30$ ns was applied, which was assumed to be nonextending. This hypothesis was tested by comparing the deadtime correction for 30-ns and 1-μs effective deadtime, and no systematic difference was obtained after correction. The deadtime correction factor $f_\tau(T)$ as a function of time of flight T is obtained from the observed total count rate $C_{\rm tot}(T)$ without applying any event selection conditions by

$$f_\tau(T) = \left(1 - \frac{1}{T_0} \sum_{t=T-\tau}^{T} C_{\rm tot}(t)\right)^{-1}, \quad (4)$$

where T_0 is the number of time-of-flight bunches. In the end, the deadtime correction is at maximum 0.4% in the peaks of the large resonances at low energy.

III. ANALYSIS OF THE DATA

A. The capture yield

The observable accessible with this experiment is the capture yield $Y(E_n)$, which is the fraction of incident neutrons that induce an (n,γ) reaction, and is related to the observed spectra in the following way:

$$Y(E_n) = N \times \frac{C_W(E_n) - B_W(E_n)}{\phi(E_n) \times \epsilon(E_n)}, \quad (5)$$

where $C_W(E_n)$ and $B_W(E_n)$ are, respectively, weighted counts and background, $\phi(E_n)$ is the number of neutrons in the sample, $\epsilon(E_n)$ is the detection efficiency, which for weighted counts is equal to the excitation energy $(S_n + E_n)$ according to Eq. (3) and N stands for the absolute efficiency normalization. The capture yield without multiple scattering corrections is related to the (n,γ) and total reaction cross sections $\sigma_{n,\gamma}(E_n)$ and $\sigma_t(E_n)$ by

$$Y(E_n) = (1 - e^{-n \times \sigma_t(E_n)}) \times \frac{\sigma_{n,\gamma}(E_n)}{\sigma_t(E_n)}, \quad (6)$$

where n is the sample density in atoms/b. The first factor is usually called self-shielding, and expresses the attenuation of neutron density along the sample. The second factor is the probability of the (n,γ) reaction occurring given that the neutron has interacted.

B. Background estimation

A number of background contributions to the observed counts were identified and they are shown in Fig. 7 together with the measured spectrum of the ^{241}Am sample. These contributions were due to the radioactivity of the sample, neutron capture and neutron scattering on the aluminium canning and on the Al_2O_3 matrix, in-beam photons, and ambient radiation.

The sample's activity was measured with a beam-off run, and normalized to acquisition time. The aluminium canning was placed alone in the beam for estimating capture

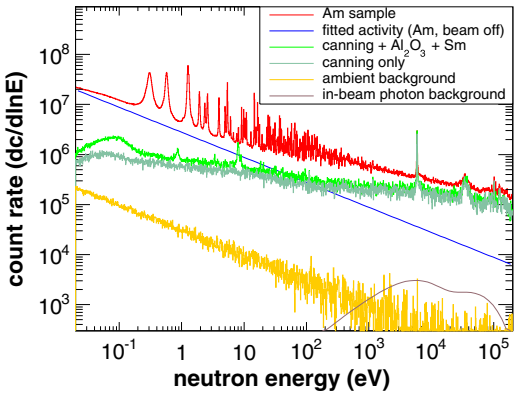

FIG. 7. (Color online) The measured ^{241}Am spectrum together with the various measured and calculated scaled background components. The count rate is expressed in a width-independent logarithmic equidistant binning.

and neutron scattering sensitivity, and this spectrum was normalized to the number of received neutrons.

The estimation of the background component due to the Al_2O_3 matrix using a measurement with the dummy sample could not be used at thermal energies. A contamination by Sm was found in the dummy spectrum only, visible by its high thermal cross section and characteristic resonances, and estimated at about 3×10^{-9} atoms/b. After examination by x-ray photography, it appeared that the dummy sample was broken in pieces and glued together, explaining the presence of Sm as a component in the used glue. Since the dummy sample could therefore not be used at low energies, the capture contribution of Al_2O_3 was instead simulated with a SAMMY [51] calculation and used as a background in the resolved resonance region. The uncertainty of the nuclear data on O and Al isotopes was neglected. Sensitivity to scattered neutrons is a possible source of remaining background in the resolved resonance region, but it is negligible on the resonance peaks. In the unresolved resonance range, the measurement of the dummy Al_2O_3 sample was used, because the small amount of Sm contributes to the count rate only significantly at low neutron energy.

The background from the 2.2-MeV in-beam photons from thermal neutron capture on hydrogen from water surrounding the spallation target has been a major source of background at n_TOF in the past. However the recent use of borated water as a moderator has strongly reduced this component, because of the very high ^{10}B(n,α) cross section at thermal neutron energies. This reaction releases a 480-keV photon with a 0.94 probability, but the corresponding Compton edge of 310 keV means that most of the energy deposit of these photons is below the applied threshold.

Runs were also taken with in-beam neutron filters of W, Al, and Co, removing all neutrons from the beam at large (black) resonances at 4.2, 18.8, 132 eV and 34.8 keV, giving access to the remaining background. When comparing the spectrum of the ^{241}Am sample with the neutron filters, and the sum of all background components except in-beam photons, the count rates were identical within the uncertainties at the black resonance energies meaning that the contribution from the in-beam photons could be neglected for the present configuration of the moderator with borated water. This was also confirmed by the expected count rate for this background, shown in Fig. 7, which was calculated from the analytical form of this background, fitted to a measured spectrum of Pb after applying capture corrections and normalization.

Finally, the ambient background (no beam, no sample) was measured and normalized to the acquisition time. The total background $B_W(E_n)$ in Eq. (5) was calculated as

$$B_W = \frac{f_{\mathrm{Am}}}{f_{\mathrm{can}}}\left(C_{\mathrm{can}} - \frac{T_{\mathrm{can}}}{T_{\mathrm{amb}}}C_{\mathrm{amb}}\right) + \frac{T_{\mathrm{Am}}}{T_{\mathrm{act}}}C_{\mathrm{act}}, \qquad (7)$$

where C_{can}, C_{amb}, and C_{act} are the measured weighted time-of-flight spectra corresponding respectively to the canning with beam, ambient (no sample, no beam) and the activity (^{241}Am sample, no beam), with corresponding acquisition times T_{Am}, T_{can}, T_{amb}, T_{act}, and incident integrated neutron intensities f_{Am} and f_{can}.

C. Normalization

From the background subtracted count rate, the yield was calculated using Eq. (5). The incident neutron fluence $\phi(E_n)$ was derived from an evaluation based on long-term measurements with several detectors [52] and corrected for the transmission through the in-beam neutron flux detectors. This flux was normalized to the actual geometrical interception of the beam by the sample at 4.9 eV. To account for the absolute level of the neutron flux and for the absolute efficiency and geometry used for the weighting function, the normalization factor N was obtained by measuring a 250-μm-thick ^{197}Au target with the same diameter and in the same setup as the ^{241}Am sample. For this thickness the resonance at 4.9 eV is saturated in the capture yield, which reduces the impact of uncertainties on the resonance parameters during the fit of the

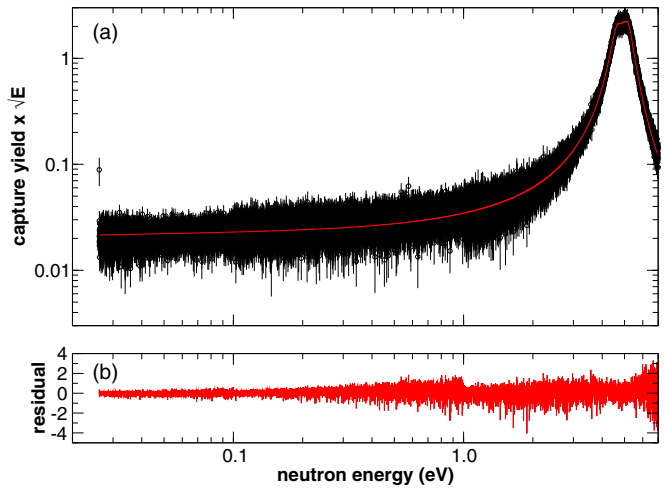

FIG. 8. (Color online) The ^{197}Au(n,γ) capture yield and the fit of the normalization with SAMMY, using fixed resonance parameters from JEFF-3.1.2 [31]. The y axis is multiplied by $\sqrt{E(\mathrm{eV})}$ for a better view of the thermal region. The lower panel shows the residual of the fit, defined as the difference of the experimental yield and the fit, divided by the uncorrelated weighted uncertainty of the data points.

normalization with SAMMY, using the resonance parameters of JEFF-3.1.2 [31]. The normalization was fitted only in the small energy range from 4.55 to 5.25 eV around the saturated resonance. From this fit an uncertainty of 1% was obtained. By extrapolating the low energy part as shown in Fig. 8, the thermal capture cross section of Au, considered a standard, was reproduced within 0.7%.

At 4.9 eV, this normalization accounts for both beam interception and the absolute efficiency normalization. One final correction is the energy dependence of the beam interception factor, however no experimental data nor numerical simulations provided the accuracy needed for this analysis. Hence, the energy dependence of the beam interception factor was not taken into account in this work.

IV. RESULTS

A. Thermal cross section

From the normalized ^{241}Am capture yield, the value of the thermal cross section was estimated. Once the resonances were adjusted individually (see Sec. IV B), the capture yield was fitted from 26.3 to 100 meV, with one bound state at the mirror energy of the first resonance, with the scattering width as a free parameter. The radiative width was taken as the average of the set of observed resonances, at 44.2 meV. Then the first resonance alone was fitted on the resonance peak. The obtained values were used as starting parameters for a fit of both the bound state and the first resonance from 0.026 meV to 0.35 eV. Figure 9 shows the very low energy region of the full fit. It is interesting to note that Fig. 9 exhibits the contamination of both ^{240}Pu at 1.05 eV and ^{237}Np at 1.48 eV. The results for the two detectors analyzed separately were giving consistent results.

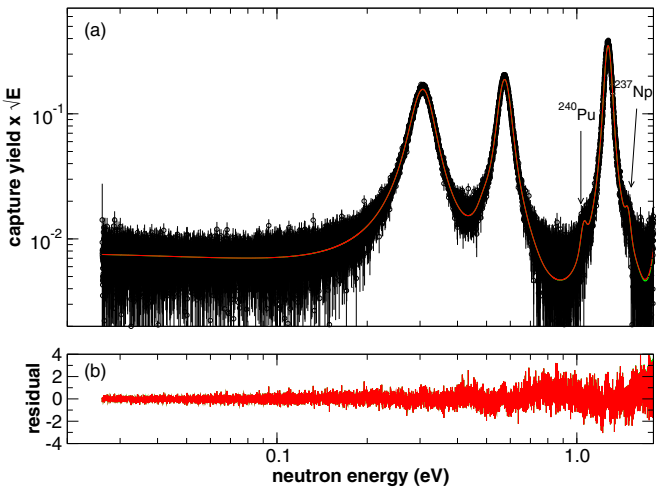

FIG. 9. (Color online) The ^{241}Am capture yield with a 300-keV threshold is fitted up to the first three resonances to obtain the thermal cross section value. The y axis is multiplied by $\sqrt{E(eV)}$ for convenience, to allow a better view of the thermal region. The lower panel shows the residual of the fit, defined as the difference of the experimental yield and the fit, divided by the uncorrelated weighted uncertainty of the data points.

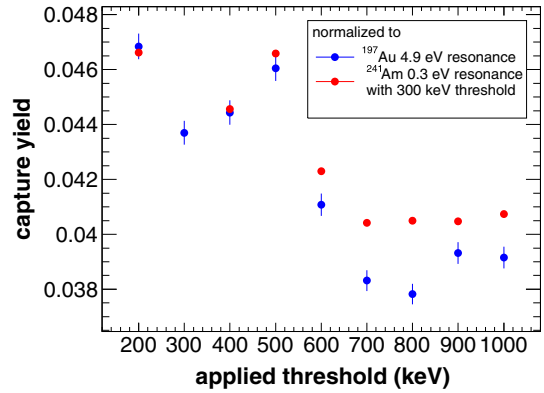

FIG. 10. (Color online) Comparison of the thermal capture yield for different thresholds, normalized to the 4.9-eV Au resonance with the same threshold (in red), and normalized to the 0.3-eV ^{241}Am resonance (in blue) which itself is normalized to Au with a threshold of 300 keV.

The influence of the detection threshold on the weighting function and resulting normalization was studied by applying different thresholds ranging from 200 keV to 1 MeV. The yield was normalized either to the first resonance of ^{241}Am, comparing similar γ-ray cascade spectra, and to the 4.9-eV resonance of Au with a different γ-ray cascade spectrum. The two detectors always provided consistent results for a given threshold.

The result of the comparison of all thresholds (with counts summed for both detectors) is shown in Fig.10. In this figure, the thermal capture yield at 25.3 meV with a 300-keV threshold was normalized to the 4.9-eV ^{197}Au resonance as described in Sec. III C. The resulting uncertainty of 1% is entirely due to the fit of the Au resonance which is dominated by counting statistics. The yields for other thresholds were normalized either to the yield on the first resonance of ^{241}Am, or normalized to ^{197}Au extracted at the same threshold. The interest in comparing the two normalization procedures lies in the bias induced by the weighting function procedure, especially at large thresholds. Indeed, starting from a threshold of 600 keV, the two differently normalized thermal capture yields start to diverge significantly.

The yields normalized to the first ^{241}Am resonance with a 300-keV threshold are only sensitive to the background, which is dominant at thermal neutron energy. In Fig. 10, the threshold dependence of the capture yield is shown for both normalization techniques, indicating that the differences on the thermal capture yield are probably due to the effect of the weighting function on the background at thermal energies. Indeed, the background/signal ratio varies from 0.93 when using a threshold of 200 keV to 0.82 with a 1-MeV threshold. At these energies most of the background is due to the the radioactivity of the sample, and notably the response to the 2235-keV γ ray, as shown in Fig. 3.

This shows that the background/signal ratio could fully explain the discrepancies observed at thermal energy, independent of the threshold. The final adopted value of the thermal cross section, obtained from the resonance parameters, was $\sigma_\gamma(25.3\ \text{meV}) = 678 \pm 68$ b. The extracted Westcott factor is

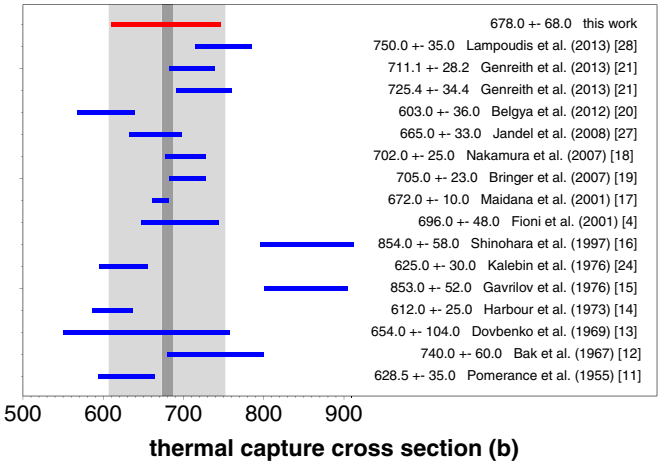

FIG. 11. (Color online) An overview of the experimental thermal total neutron capture cross section values as extracted from experimental data library EXFOR. The larger gray band indicates the average and standard deviation of the central values (698.5 and 72.7 b). The smaller gray band corresponds to the weighted mean and its uncertainty, excluding values without uncertainty (679.5 and 6.5 b).

0.995. The adopted uncertainty of 10% is based on the spread observed in Fig. 10 below the 500-keV threshold. In Fig. 11 this thermal value is plotted together with previously reported values. It should be mentioned that the present experiment was not optimized for the thermal region, but for the resonance region.

B. Resolved resonance region (RRR)

The obtained yield with 300-keV threshold was used for a resonance shape analysis using the *R*-matrix code SAMMY [51] in the Reich-Moore approximation. The analysis included multiple scattering and self-shielding corrections, and used the free gas model for Doppler broadening with an effective temperature of 296 K. The n_TOF phase-I resolution function as given in SAMMY [51] was used in the analysis and the neutron energy calibration was adjusted to the 4.9-eV resonance in Au using parameters from JEFF-3.1.2 [31], resulting in an effective flight path length of $L = 184.21 \pm 0.06$ m. Resonances were fitted individually whenever possible, and overlapping resonances forming multiplets were fitted together. The γ partial width Γ_γ was let free for the first three large resonances, where it is expected to be sensitive to small variations of the parameters (see Table III).

For the remaining set of states the value of Γ_γ was fixed to the average value $\Gamma_\gamma = 45.79$ meV of the first three resonances. The fission widths and the spins for the existing resonances were taken from JEFF-3.1.2 [31]; for the negative resonance the same spin as the first positive resonance was chosen. For new resonances a spin of either $J = 2$ or $J = 3$ was arbitrarily chosen according to a $2J + 1$ distribution, as well as an average fission width of $\Gamma_f = 0.3597$ meV. In the energy range up to 150 eV, the upper limit of all present evaluations, a number of 15 new resonances were found. From 150 to 320 eV, for which currently no resonances are present

TABLE III. The resonance parameters for the first three resonances. Only uncertainties due to counting statistics have been used in the data, and the uncertainties resulting from the fit correspond to the square root of the diagonal terms only. The correlation factor between Γ_n and Γ_γ from the fit was lower than 0.25.

Energy (eV)	J ($\hbar$)	Γ_n μeV	Γ_γ (meV)
−0.306	3	275.3 ± 2.0	45.79
0.306	3	49.1 ± 0.1	45.35 ± 0.3
0.575	2	116.7 ± 0.3	44.41 ± 0.5
1.272	3	290.0 ± 0.9	47.16 ± 0.3

in evaluations, a total number of 157 new resonances were found and analyzed. Figure 12 shows the full range of resolved resonance data together with the fitted resonances. Table IV gives the full list of resonance parameters obtained in this analysis. New resonances as compared to JEFF-3.1.2 [31] are marked with a *.

The resonance integral

$$I = \int_{E_c}^{\infty} \sigma_{n,\gamma}(E) \times \frac{dE}{E} \tag{8}$$

was calculated with $E_c = 0.5$ eV. With the new resonance parameters this gave $I = 1425.0$ b. It should be noted that the traditional choice of 0.5 eV for the lower bound of the integral is, in the case of ^{241}Am, a source of uncertainty, since the first resonance is at 0.3 eV and the second one at 0.57 eV. This means that a very slight change in the resonance parameters will have a very significant effect on the resonance integral, if the lower bound is chosen at 0.5 eV. For further discussion, see Lampoudis *et al.* [28].

C. Statistical analysis

The newly fitted resonance parameters were used to perform a statistical analysis of this new set of states. First, the resonances were all checked to be *s* waves, i.e., carrying $\ell = 0$ angular momentum in the entrance channel. This test is carried out by a statistical approach, based on Bayesian probabilities, inspired by the work of Bollinger and Thomas [53] on ^{238}U and more recently applied to ^{99}Tc [54], ^{232}Th [48], and ^{241}Am [28]. The quantity of interest is the probability of a resonance being a *p* wave, given the observed scattering width $g\Gamma_n$. It can be expressed using Bayes' theorem, and the assumption that only *s* and *p* waves are present in the observed set of states. The detailed mathematical treatment has been discussed by Gyulassy *et al.* [55], and is based on a weighted combination of Porter-Thomas distributions with one or two degrees of freedom, respectively for $\ell = 0$ and $\ell = 1$ states. Taking neutron strength functions from Ref. [56], this analysis yields no *p*-wave resonance in the observed set of ^{241}Am resonances, i.e., all resonances have $P(\ell = 1|g\Gamma_n) = 0$.

The average spacing D_0 and strength function S_0 were extracted from the present set of *s*-wave resonances. To that end, the Porter-Thomas distribution was used again, expressing the number of $\ell = 0$ states $N(x_t)$ with $x = \frac{g\Gamma_n^0}{\langle g\Gamma_n^0 \rangle}$ larger than a

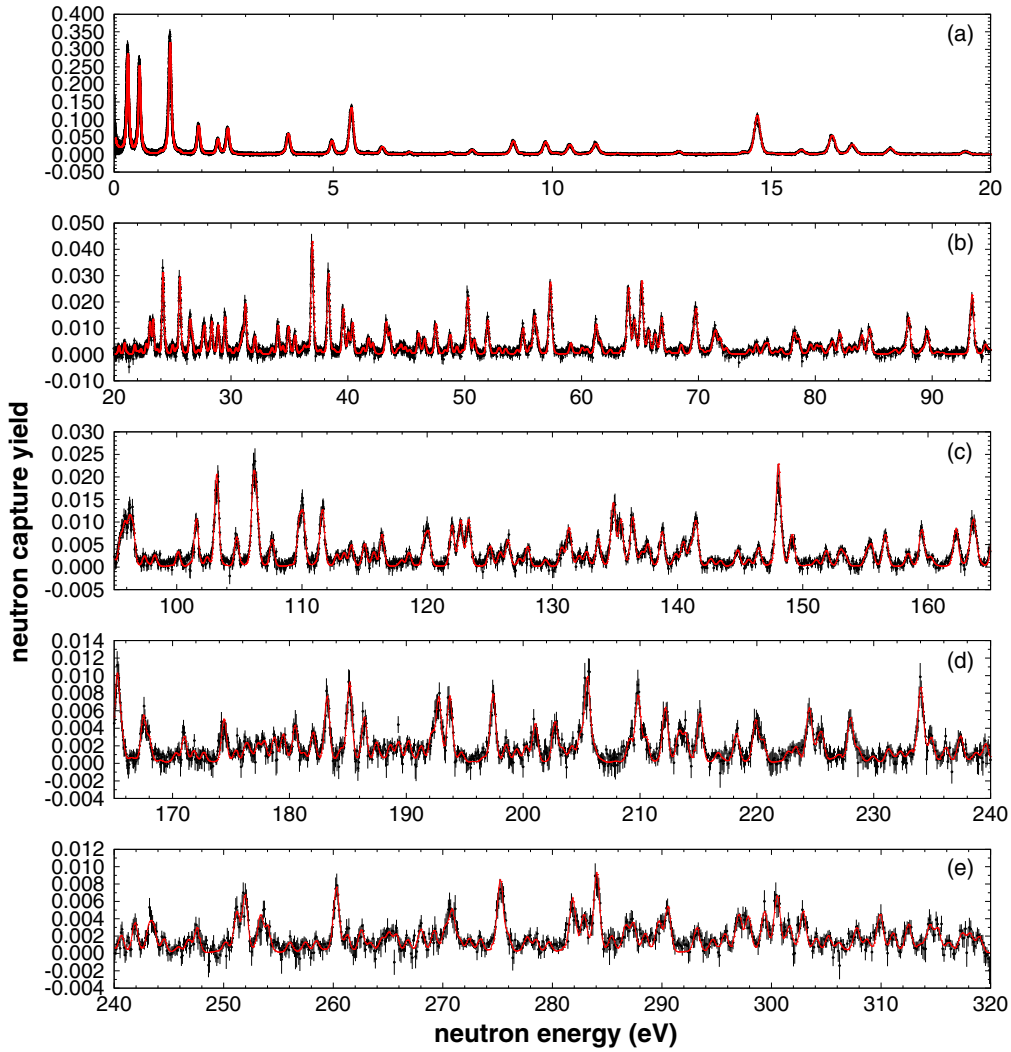

FIG. 12. (Color online) The resolved resonance range analyzed in this work. The blue points are the experimental data, and the red line is the fit performed with SAMMY. The first panel has 500 bins per decade, whereas the following have 5000 bins per decade.

certain threshold x_t as

$$N(x_t) = N_0 \int_{x_t}^{\infty} \sqrt{\frac{2}{\pi x}} \frac{1}{2} e^{-x/2} dx = N_0[1 - \mathrm{erf}(\sqrt{x_t/2})] \tag{9}$$

with N_0 the expected total number of s waves in the set. Assuming that all the resonances are observed above a certain threshold x_t, one can fit this function to the experimental distribution in order to get N_0 and $\langle g\Gamma_n^0 \rangle$ (Fig. 13).

From the fitted values N_0 and $\langle g\Gamma_n^0 \rangle$ the quantities D_0 and S_0 were extracted as

$$D_0 = \frac{N_0}{\Delta E}, \quad S_0 = \frac{\langle g\Gamma_n^0 \rangle}{D_0}. \tag{10}$$

In the resolved energy range up to 320 eV this procedure yields $D_0 = 0.52 \pm 0.03$ eV and $10^{-4} S_0 = 1.20 \pm 0.01$, with a correlation coefficient of -0.90. The uncertainties associated to these results come from the relative stability of the analysis with respect to variations of the $g\Gamma_n$ threshold which was varied in order to include a fraction of the observed resonances ranging from 1/2 up to 4/5.

D. Unresolved resonance region (URR)

Above 320 eV neutron energy, the resonances were overlapping and no satisfactory fit of individual resonances could be performed. Therefore this region was considered the start of the unresolved resonance range. The upper limit for this analysis was chosen at 150 keV as a consequence of the recovery time of the C_6D_6 detectors after the gamma flash. At 150 keV, the fission cross section is 70 times lower than the capture cross section in all evaluations (around 18 mb against 1.25 b) and is expected not to contribute significantly to the background. Also, inelastic scattering is not an issue, because of the 300-keV effective threshold used for the event selection. In order to get the unresolved capture yield, the data were binned in 40 bins per energy decade to average most of the resonance structure, while still keeping the sensitivity to the global energy dependence.

TABLE IV. The resonance parameters above 1.9 eV obtained by this work. The common relative uncertainty on the resonance energy is 6.5×10^{-4} and is completely determined by the uncertainty on the flight path length through $\Delta E/E = 2\Delta L/L$. New resonances are marked with a *. Note that each line in the table contains the parameters of two resonances.

Energy (eV)	J ($\hbar$)	Γ_n (μeV)	$d\Gamma_n$ (μeV)	Energy (eV)	J ($\hbar$)	Γ_n (μeV)	$d\Gamma_n$ (μeV)
1.922	3	104.0	0.6	2.365	2	93.2	0.9
2.589	3	136.7	0.9	3.971	2	261.4	2.3
4.966	3	160.1	1.8	5.412	2	936.0	6.5
5.926	2	13.1	2.1	6.116	3	115.2	2.1
6.736	3	38.5	1.7	7.660	2	65.4	2.9
8.167	3	106.2	2.7	9.107	2	489.1	6.8
9.845	3	365.7	5.6	10.07	2	55.2	4.1
10.40	3	300.1	4.9	10.99	2	502.2	8.6
11.49	3	33.2	3.5	12.19	3	23.9	3.4
12.88	2	176.8	6.9	13.90	3	36.0	4.2
14.36	2	125.9	8.1	14.68	3	2061.8	22.7
15.68	2	339.6	10.7	16.39	3	1103.2	16.2
16.85	2	838.3	16.3	17.72	3	388.5	10.0
19.43	2	310.8	12.0	20.38	3	41.2	7.4
20.88	3	115.3	7.2	21.75	2	146.7	11.6
22.28	3	57.8	7.5	22.73	2	163.7	12.4
23.06	3	382.9	13.5	23.33	2	603.2	20.0
24.18	3	1092.0	23.6	24.38	3	76.2	11.9
25.31	2	82.3	14.8	25.63	3	1124.1	23.8
26.48	2	627.9	27.9	26.69	3	203.8	15.8
27.18*	3	57.1	9.3	27.56	2	322.3	22.6
27.74	3	410.9	19.8	28.11*	3	50.8	13.3
28.35	2	750.0	26.0	28.90	3	476.7	17.5
29.50	3	639.9	20.5	29.90	2	107.3	17.9
30.77	3	143.7	15.9	30.99	2	517.7	31.8
31.24	3	932.7	28.0	31.57*	3	58.2	12.1
32.04	2	483.8	25.3	32.45*	3	69.2	12.7
33.50	3	114.1	16.4	34.02	2	850.7	33.0
34.43	3	163.4	16.2	34.93	2	846.0	33.8
35.48	3	419.1	20.9	36.01*	2	94.3	24.4
36.26	3	177.5	19.8	36.53	2	203.6	28.7
36.97	3	2930.2	62.1	37.61*	3	87.2	15.6
38.36	2	3107.1	78.5	38.76	3	79.0	21.0
39.61	3	1221.7	37.3	40.06	2	765.8	41.9
40.40	3	844.8	35.0	41.27	2	166.4	31.6
41.77	3	432.6	25.6	42.12	2	428.7	36.5
43.28	3	960.9	40.3	43.59	2	879.7	44.7
44.54	3	330.2	28.9	44.90	3	211.0	25.0
45.28*	2	175.8	37.4	46.04	2	955.0	52.5
46.58	3	483.8	32.0	47.54	2	1499.3	58.3
48.31*	2	182.1	32.1	48.76	3	682.9	37.1
49.32	3	270.9	28.0	50.28	2	2896.0	96.5
50.83	3	531.3	34.0	51.98	2	1922.7	72.6
52.93	3	262.5	28.6	53.50	2	311.2	38.1
54.49	3	161.8	31.9	55.00	2	1579.7	70.8
55.59	3	308.6	37.4	55.98	2	2279.8	99.2
56.24	3	609.6	51.3	57.35	3	3421.3	101.4
59.08	2	727.1	66.9	60.06	3	236.4	43.7
60.46	2	361.7	55.9	61.26	3	1472.4	63.6
61.62	2	858.4	66.2	62.44	3	179.7	34.2
63.47	3	291.0	35.5	64.04	2	5586.2	187.0
64.55	3	1830.1	74.5	65.18	2	6411.1	203.8
65.75	3	1161.2	75.2	66.31	2	1533.6	88.4
66.88	3	2120.7	83.6	68.54	2	767.2	69.7
69.52	3	819.5	75.0	69.82	2	4101.8	172.5
70.32*	3	162.7	43.9	70.81*	3	164.9	42.0
71.26	3	621.4	88.2	71.50	2	1767.6	129.6
71.88	3	965.6	71.5	72.38	3	372.1	48.6
74.39*	3	265.9	50.3	74.97	2	955.0	87.1
75.66	3	540.4	69.6	75.94	2	964.8	95.0
76.61*	2	245.3	77.8	77.08	3	338.9	49.5
78.23	2	2138.0	134.9	78.60	3	1043.1	77.4
79.62	3	707.1	67.5	80.12	2	905.6	105.2
80.49	3	593.6	70.5	81.22	2	524.1	98.0
81.51	3	905.9	85.5	82.13	2	2305.7	143.4
82.90	3	531.0	67.3	83.38	2	696.4	95.1
84.01	3	1520.6	95.8	84.67	3	2099.8	102.8
86.87	2	525.6	85.3	87.50	3	375.7	59.7
88.01	2	4959.2	223.7	89.19	3	363.6	64.7
89.62	2	3021.2	175.2	90.46*	3	198.9	49.3
93.46	3	5937.2	234.7	94.58*	3	906.7	93.9
95.00	2	499.4	119.8	95.54	3	1502.1	133.1
95.89	2	3295.3	248.7	96.25	3	2493.5	197.3
96.56	2	3126.7	236.7	97.44	3	569.1	81.1
98.27	3	644.3	74.0	100.14	2	1130.1	138.7
101.61	3	3060.3	165.0	102.46	2	748.2	113.8
103.24	3	6767.8	279.3	104.82	3	1899.6	149.1
106.18	2	9650.9	518.1	106.47	3	3212.4	247.3
107.65	2	2684.5	231.1	109.83	3	2779.1	228.0
110.15	2	5273.0	387.3	111.41	3	614.6	200.3
111.69	2	6237.5	382.8	112.82	3	831.4	99.9
113.39	2	1280.7	156.4	114.00	3	1508.6	144.0
115.05	3	1653.9	146.5	115.78	2	1385.7	181.9
116.45	3	2550.2	186.3	118.00	2	638.0	154.2
118.59	3	1075.0	130.3	119.83	2	2757.9	266.3
120.17	3	2530.9	185.9	122.05	2	5009.7	337.8
122.73	3	4007.9	232.3	123.37	3	3997.7	222.4
125.08	2	2452.7	230.7	125.89	3	1095.4	166.6
126.51	2	3387.4	249.9	127.43	3	619.4	112.7
128.08	2	2560.1	256.6	129.50	3	557.0	117.1
130.80	2	2390.9	260.9	131.39	3	3570.9	243.2
132.19	3	915.8	159.4	132.78	2	1926.9	240.6
133.73	3	2548.6	203.8	134.93	2	9964.3	600.6
135.53	3	4727.5	304.4	136.48	2	7564.7	529.0
137.19	3	1220.4	164.5	137.69	2	2987.5	317.6
138.83	3	3557.8	227.1	139.90	3	1157.1	160.3
140.52	2	3632.5	334.5	141.10	3	1684.5	208.2
141.54	2	7583.0	506.5	142.72*	2	1082.0	177.4
143.47	3	604.9	156.2	144.87	2	2495.5	212.4
145.74	3	700.8	141.7	146.55	2	2982.9	260.8
148.14	3	13181.9	656.0	149.23	3	3745.0	296.5
151.13*	2	996.0	209.6	151.95*	2	2563.2	335.0
153.07*	2	2599.2	311.4	153.47*	2	1553.5	264.9
155.17*	2	2081.5	321.2	155.55*	3	2436.6	277.4
156.67*	2	5872.8	428.0	158.48*	3	1448.1	223.7
159.59*	2	7206.2	509.9	160.26*	2	1635.0	259.1
162.32*	3	5180.8	340.0	163.45*	3	1458.9	386.6
163.72*	2	8307.7	1045.0	164.02*	3	845.4	258.9
165.34*	3	6231.3	445.5	165.74*	3	1706.6	278.7

TABLE IV. (*Continued.*)

Energy (eV)	J ($\hbar$)	Γ_n (μeV)	$d\Gamma_n$ (μeV)	Energy (eV)	J ($\hbar$)	Γ_n (μeV)	$d\Gamma_n$ (μeV)
166.49*	3	220.2	135.3	167.59*	2	4604.9	423.0
168.10*	2	2239.3	301.8	170.36*	3	572.5	135.6
171.09*	3	1725.8	211.5	171.90*	3	792.3	175.6
172.74*	3	674.8	167.7	174.49*	2	4694.8	485.0
176.35*	3	1031.3	250.5	176.65*	3	612.4	262.5
175.51*	3	786.4	139.9	177.39*	2	1800.0	295.6
177.93*	2	2226.3	319.2	178.79*	3	1866.0	253.0
179.56*	3	2119.5	226.4	180.58*	2	4141.9	447.3
181.30*	2	869.9	263.9	182.12*	3	2317.1	252.2
183.32*	2	8322.8	690.9	184.50*	2	1237.2	387.8
185.24*	3	7385.4	519.5	186.50*	2	5500.7	537.3
187.53*	3	1582.0	223.5	188.72*	2	1903.7	303.8
189.43*	3	1573.4	231.6	190.28*	2	2492.4	338.8
191.36*	2	1849.1	295.1	192.26*	3	2218.3	297.3
192.87*	3	5970.3	454.7	193.83*	2	9098.2	771.8
194.81*	2	1143.2	282.9	197.53*	3	6748.5	512.4
198.65*	2	2189.7	400.3	199.53*	2	1600.0	294.0
200.34*	3	1277.9	229.3	201.14*	3	3635.1	421.0
202.83*	2	5608.2	652.1	203.47*	3	1196.8	257.5
204.25*	2	1845.5	329.8	205.60*	3	9262.9	797.6
206.16*	2	1798.6	366.6	204.98*	3	2174.9	312.4
209.21*	2	2890.5	420.1	209.95*	3	7140.1	595.9
210.65*	3	2252.1	355.1	212.28*	2	8765.9	810.7
213.45*	3	2896.6	414.1	214.01*	3	2874.5	474.1
215.25*	2	7755.2	801.8	216.77*	2	1095.8	281.1
218.37*	2	4411.7	502.9	220.01*	3	4522.5	473.8
220.66*	3	2300.8	364.8	222.78*	2	1488.0	485.7
223.44*	2	2280.4	421.1	224.60*	2	9290.7	880.9
225.34*	3	1637.1	423.4	225.69*	3	2590.1	582.9
227.12*	3	743.6	257.2	228.12*	3	5162.7	548.3
228.78*	3	1374.4	436.2	230.02*	3	576.6	218.3
231.37*	2	1920.4	399.5	232.38*	2	1680.8	381.1
233.23*	2	1445.4	424.3	234.15*	3	10117.8	806.7
235.04*	3	2842.4	396.3	236.30*	2	2423.8	553.5
237.55*	3	3034.0	397.6	238.86*	2	1507.5	451.6
239.71*	2	2968.7	716.6	240.78*	3	2034.4	397.4
242.04*	2	5493.0	716.5	243.31*	3	2918.2	518.6
243.74*	3	2921.2	498.6	244.67*	3	1643.7	323.8
245.96*	3	614.6	270.6	246.91*	2	2084.2	492.7
247.71*	2	4696.6	877.6	250.29*	2	1726.4	478.8
251.32*	2	7647.9	963.2	252.09*	2	12436.5	1339.5
253.49*	3	4940.7	678.2	254.16*	3	3569.8	494.8
256.17*	2	1910.4	500.7	257.60*	3	1298.6	368.3
258.58*	3	1538.6	367.9	260.43*	2	16511.9	1602.4
261.41*	3	2378.6	562.2	262.70*	2	4614.4	842.7
263.50*	2	1783.0	495.4	264.58*	3	1733.6	466.3
265.22*	2	3743.0	797.9	265.89*	3	2575.1	587.1
266.95*	2	2510.6	523.7	268.09*	2	3548.1	1103.9
268.30*	2	1441.9	928.0	269.36*	3	3214.8	573.9
270.37*	2	4678.5	825.7	271.00*	2	9220.4	1314.1
271.64*	3	1750.3	396.6	272.56*	3	1984.3	347.9
273.59*	3	1936.5	471.9	275.40*	2	21815.5	2185.9
276.13*	2	3560.7	795.7	277.85*	3	2169.6	401.4
278.65*	2	2802.4	693.4	279.82*	2	2258.8	393.7
282.00*	2	14728.7	1598.0	283.02*	2	8998.6	1082.7
284.21*	3	16835.4	1484.8	285.56*	3	2565.8	761.9
286.84*	2	5811.8	1061.2	287.54*	2	7150.7	1128.3

TABLE IV. (*Continued.*)

Energy (eV)	J ($\hbar$)	Γ_n (μeV)	$d\Gamma_n$ (μeV)	Energy (eV)	J ($\hbar$)	Γ_n (μeV)	$d\Gamma_n$ (μeV)
288.62*	2	4280.1	719.7	289.86*	3	5000.4	709.4
290.72*	2	12628.9	1389.0	293.36*	3	4178.9	606.8
294.78*	3	2121.0	448.1	295.90*	2	4483.7	790.7
297.17*	3	6458.3	797.3	298.04*	3	6344.7	807.9
299.53*	2	10939.7	1476.0	300.70*	3	11420.9	1200.3
301.79*	2	6801.4	1081.4	303.06*	3	8061.0	803.4
304.23*	2	3407.0	802.4	305.36*	3	2963.0	566.5
306.28*	3	1445.0	501.4	307.94*	2	6682.7	1129.1
308.84*	2	3180.2	803.5	310.09*	3	7744.4	963.7
311.25*	2	4814.6	971.8	312.70*	3	5241.7	738.7
313.80*	2	1728.5	750.2	314.62*	2	7162.4	1292.3
315.34*	3	4601.0	762.4	316.33*	2	2389.3	768.2
317.57*	3	3396.3	719.5	318.28*	2	4915.5	1375.8
319.13*	3	3080.2	602.1				

The main source of background in this region comes from neutron scattering and capture on the dummy sample and the canning while the contribution from the sample activity becomes negligible. Figure 14 shows the spectrum with the Am sample and the estimated backgrounds with and without filters in the URR. As the black resonance of the ^{27}Al filter at 34.8 keV was used for this analysis, the estimated total background is compatible with the total signal, which strengthens the background subtraction procedure. Within the uncertainties no additional backgrounds can be estimated.

The average capture cross section $\langle\sigma_{n,\gamma}(E_n)\rangle$ was obtained from the average capture yield $\langle Y(E_n)\rangle$ using Eq. (6) in the form

$$\langle Y(E_n)\rangle = f(E_n) \times n \times \langle\sigma_{n,\gamma}(E_n)\rangle, \tag{11}$$

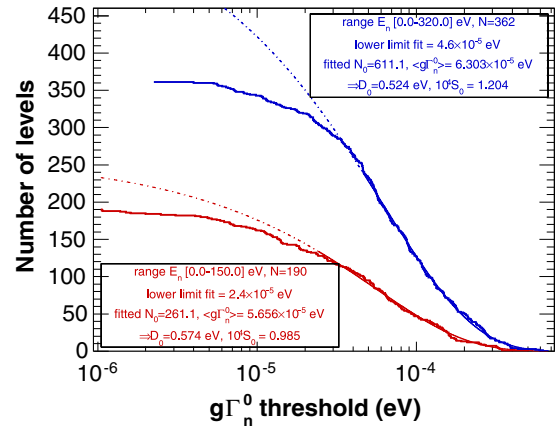

FIG. 13. (Color online) The cumulative Porter-Thomas distribution for the s-wave resonances fitted (solid curve) by Eq. (9) and extrapolated to zero threshold (dashed curve), both for the set of observed resonances in this work (blue) and the evaluated data from JEFF-3.1.2 (red). The obtained values for D_0 and S_0 depend on the choice of the threshold, here chosen such that 2/3 of the resonances are included in the fit.

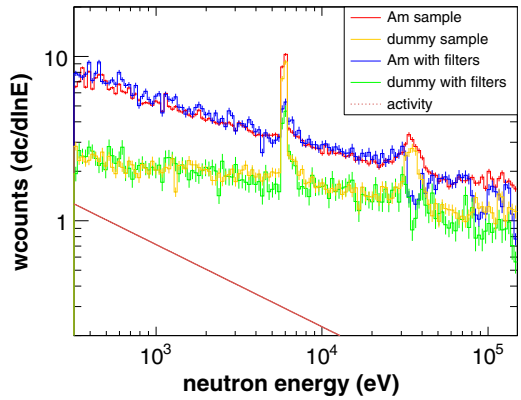

FIG. 14. (Color online) The total signal and background components in the URR with and without the filters in the beam.

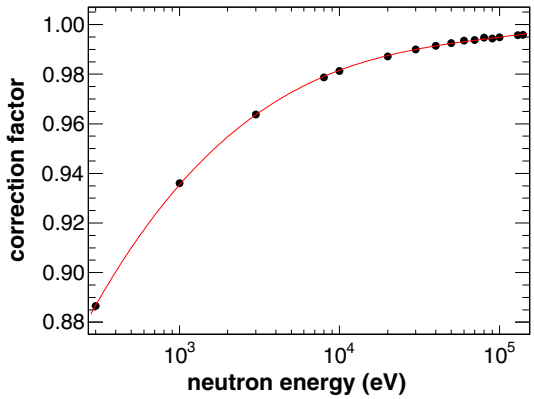

FIG. 15. (Color online) The calculated correction factor obtained with the code SESH [57] and the interpolation curve $f(E_n)$.

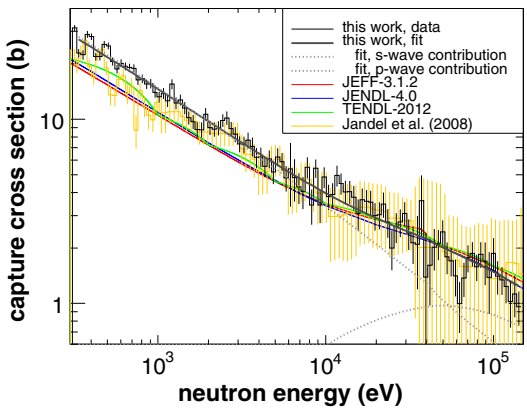

FIG. 16. (Color online) The final unresolved cross section compared to previous data and evaluations.

TABLE V. The neutron strength functions S_ℓ and average radiation widths $\langle\Gamma_\gamma\rangle_\ell$ fitted by FITACS to the average measured cross section.

$\ell = 0$	$\ell = 1$
$S_0 = (1.44 \pm 0.02) \times 10^{-4}$	$S_1 = (1.14 \pm 0.10) \times 10^{-4}$
$\langle\Gamma_\gamma\rangle = 0.043 \pm 0.002$ meV	$\langle\Gamma_\gamma\rangle = 0.045 \pm 0.002$ meV

where $f(E_n)$ is a statistical correction factor which accounts for both self-shielding and multiple scattering corrections. This factor is the result of complex processes which usually cannot be determined analytically, but in general is determined using a Monte Carlo approach. To that end, the code SESH [57] was used to generate artificial resonances, based on the information on level densities and strength functions and extract $f(E_n)$ at specific energies E_n. The interpolated curve as shown in Fig. 15 was then used in Eq. (11) to obtain the average capture cross section $\langle\sigma_{n,\gamma}(E_n)\rangle$.

Figure 16 shows the comparison of the average cross section obtained by this work, together with the parametrization performed by the FITACS module included in SAMMY, and current evaluations, as well as the data of Jandel *et al.* [27], the only other available experimental dataset. The result of the calculation by FITACS is shown in Table V, using fixed values of $D_0 = 0.53$ eV (see Sec. IV C) and $D_1 = D_0/2$.

Slightly higher values for S_ℓ were found in this region as compared to the results of the statistical analysis of Sec. IV C. This may be explained by the fact that the neutron strength function could show some moderate energy dependence, in addition to the fact that the method of obtaining S_ℓ is different in the two energy regions.

The present capture cross section seems to be higher than the measurement of Jandel *et al.* [27] below 10 keV but agrees within the uncertainties at higher energies. This does not seem to originate from an issue in normalization, since the capture yield of ^{197}Au showed consistency with energy, and the first resonances are not systematically larger than previous estimations. Concerning the background estimation, the filters did not show any time independent residual contribution, and measured neutron scattering on the Al_2O_3 matrix was taken into account properly in the URR (although it was unusable in the RRR because of strong Sm resonances). Finally, this increase is consistent with the increase of the neutron strength function observed in the RRR.

V. CONCLUSIONS

The ^{241}Am(n,γ) cross section has been successfully measured at the n_TOF facility at CERN. It was possible to perform a resolved resonance analysis up to 320 eV neutron energy, increasing significantly the present limit of 150 eV of the RRR in current evaluations. A total number of 362 resonances were analyzed, including 172 new resonances of which 157 were in the extended RRR between 150 and 320 eV.

The thermal capture cross section was determined at 678 ± 68 b. The large background/signal ratio in the thermal

energy region resulted in the 10% uncertainty making this measurement compatible with many previous measurements.

From a statistical analysis, the level density and the neutron strength function were determined. Below 150 eV, several resonances were added or strongly modified. However, for a full evaluation of the resonance region, it would be necessary to include transmission data for a combined fit, as well as accurate fission widths.

The average capture cross section has been measured and modelled from 320 eV to 150 keV, and it is systematically larger than existing evaluations, and to a lesser degree, than the data of Jandel [27]) below 10 keV. This is supported by the statistical analysis of the observed resonances, which yields a larger s-wave strength function than previously evaluated [56].

ACKNOWLEDGMENTS

This work was supported by the European Commission with the FP7 project ANDES (FP7-249671) and the French national research program GEDEPEON.

[1] S. Sala, Ph.D. thesis, University of Provence, France, 1995.
[2] S. David, A. Billebaud, M. E. Brandan, R. Brissot, A. Giorni, D. Heuer, J.-M. Loiseaux, O. Méplan, H. Nifenecker, J.-B. Viano, and J.-P. Schapira, Nucl. Instrum. Methods Phys. Res., Sect. A **443**, 510 (2000).
[3] J. L. François, J. R. Guzmán, and C. Martín-del-Campo, Nucl. Eng. Des. **239**, 1911 (2009).
[4] G. Fioni, M. Cribier, F. Marie *et al.*, Nucl. Phys. A **693**, 546 (2001).
[5] V. Berthou, C. Degueldre, and J. Magill, J. Nucl. Mater. **320**, 156 (2003).
[6] IAEA, IAEA Technical Report. Thorium Fuel Cycle - Potential Benefits and Challenges, Tech. Rep. IAEA TECDOC 1450, IAEA, 2005.
[7] E. Gonzalez, in International Conference on Nuclear Data for Science and Technology (2013) (unpublished).
[8] OECD-NEA, "Nuclear Data High Priority Request List", http://www.oecd-nea.org/dbdata/hprl/.
[9] T. Yamamoto, in *Proceedings of the 2005 Symposium on Nuclear Data* (JAEA, Tokai, Japan, 2006), pp. 7–13.
[10] G. Aliberti, G. Palmiotti, M. Salvatores *et al.*, Ann. Nucl. Energy **33**, 700 (2006).
[11] H. Pomerance, in *Physics Division Semiannual Progress Report* (ORNL, Oak Ridge, 1955), pp. 50–55.
[12] M. A. Bak, A. S. Krivohatskiy, K. A. Petrzhak, E. A. Romanov, and Ju. F. Shljamin, At. Energ. **23**, 316 (1967).
[13] A. G. Dovbenko, V. I. Ivanov, V. E. Kolesov *et al.*, Rept: Bull. Centr po Jadernym Dannym, Obninsk, No. 6, p. 42 (1969).
[14] R. Harbour, K. Mac Murdo, and F. Mc Crosson, Nucl. Sci. Eng. **50**, 364 (1973).
[15] V. D. Gavrilov, V. A. Goncharov, V. V. Ivanenko, V. P. Smirnov, and V. N. Kustov, At. Energ. **41**, 808 (1976).
[16] N. Shinohara, Y. Hatsukawa, K. Hata, and N. Kohno, J. Nucl. Sci. Technol. **34**, 613 (1997).
[17] N. L. Maidana, M. S. Dias, and M. F. Koskinas, Radiochim. Acta **89**, 419 (2001).
[18] S. Nakamura, M. Ohta, H. Harada, T. Fujii, and Y. Hajimu, Nucl. Sci. Technol. **44**, 1500 (2007).
[19] O. Bringer, I. AlMahamid, S. Chabod, F. Chartier, E. Dupont, A. Letourneau, P. Mutti, L. Oriol, S. Panebianco, and Ch. Veyssière, in *International Conference on Nuclear Data for Science and Technology-ND2007, Nice* (EDP Sciences, Les Ulis, 2007), pp. 619–622.
[20] T. Belgya, L. Szentmiklósi, Z. Kis, N .M. Nagy, and J. Kónya, IAEA Report INDC(HUN)-0037 (IAEA, Vienna, 2012).
[21] C. Genreith, M. Rossbach, Zs. Révay, and P. Kudejova, in International Conference on Nuclear Data for Science and Technology (2013) (unpublished).
[22] H. Derrien and B. Lucas, in *Proceedings of a Conference on Nuclear Cross Sections and Technology, Washington, D.C., 1975*, Natl. Bur. Stand. (U.S.) Spec. Publ. No. 425, edited by R. A. Schrack and C. D. Bowman (U.S. GPO, Washington, D.C., 1975), p. 637.
[23] T. S. Belanova, A. G. Kolesov, V. A. Poruchikov, G. A. Timofeev, S. M. Kalebin, V. S. Artamonov, and R. N. Ivanov, At. Energ. **38**, 29 (1975).
[24] S. M. Kalebin *et al.*, At. Energ. **40**, 303 (1976).
[25] L. W. Weston and J. H. Todd, Nucl. Sci. Eng. **61**, 356 (1976).
[26] G. Vanpraet, E. Cornelis, S. Raman, and G. Rohr, Radiat. Eff. **93**, 157 (1986).
[27] M. Jandel, T. Bredeweg, E. Bond *et al.*, Phys. Rev. C **78**, 034609 (2008).
[28] C. Lampoudis, S. Kopecky, O. Bouland, F. Gunsing, G. Noguere, A. J. M. Plompen, C. Sage, P. Schillebeeckx, and R. Wynants, Eur. Phys. J. Plus **128**, 86 (2013).
[29] M. B. Chadwick, M. Herman, P. Oblozinsky *et al.*, Nucl. Data Sheets **112**, 2887 (2011).
[30] K. Shibata, O. Iwamoto, T. Nakagawa, N. Iwamoto, A. Ichihara, S. Kunieda, S. Chiba, K. Furutaka, N. Otuka, T. Ohasawa, T. Murata, H. Matsunobu, A. Zukeran, S. Kamada, and J.-i. Katakura, J. Nucl. Sci. Technol. **48**, 1 (2011).
[31] A. J. Koning, E. Koning, J. Dean, E. Dupont, U. Fischer, R. A. Forrest, R. Jacqmin, H. Leeb, M. A. Kellett, R. W. Mills, C. Nordborg, M. Pescarini, Y. Rugama, and P. Rullhusen, J. Kor. Phys. Soc. **59**, 1057 (2011).
[32] J. W. T. Dabbs, C. H. Johnson, and C. E. Bemis, Nucl. Sci. Eng. **83**, 22 (1983).
[33] J. Harvey, R. Block, and G. G. Slaughter, Bull. Am. Phys. Soc. **4**, 34(M7) (1959).
[34] B. R. Leonard, Jr. and E. J. Seppi, Bull. Am. Phys. Soc. **4**, 31(K1) (1959).
[35] C. D. Bowman, M. S. Coops, G. F. Auchampaugh, and S. C. Fultz, Phys. Rev. **137**, B326 (1965).
[36] V. F. Gerasimov, Yad. Fiz. **4**, 985 (1966).
[37] S. Marrone *et al.*, Nucl. Instrum. Methods Phys. Res., Sect. A **517**, 389 (2004).
[38] J. Pancin *et al.*, Nucl. Instrum. Methods Phys. Res., Sect. A **524**, 102 (2004).
[39] F. Belloni, F. Gunsing, and T. Papaevangelou, Mod. Phys. Lett. A **28**, 1340023 (2013).
[40] C. Guerrero, U. Abbondanno, G. Aerts *et al.*, Nucl. Instrum. Methods Phys. Res., Sect. A **608**, 424 (2009).
[41] T. n_TOF Collaboration, CERN n TOF Facility: Performance Report, CERN-SL-2002-053 ECT, Tech. Rep., CERN, 2003.
[42] C. Guerrero *et al.*, Eur. Phys. J. A **49**, 27 (2013).
[43] U. Abbondanno *et al.*, Nucl. Instrum. Methods Phys. Res., Sect. A **538**, 692 (2005).

[44] C. Sage, V. Semkova, O. Bouland *et al.*, Phys. Rev. C **81**, 064604 (2010).
[45] H. Tagziria, J. Bagi, B. Pedersen, and P. Schillebeeckx, Nucl. Instrum. Methods Phys. Res., Sect. A **691**, 90 (2012).
[46] A. Krasa and A. Plompen, JRC-IRMM Technical Note Eur 24818, 2011.
[47] J. F. Briesmeister, *MCNP—A General Monte Carlo n-particle Transport Code*, Vol. LA-13709-M (Los Alamos National Laboratory, Los Alamos, 2000).
[48] F. Gunsing *et al.* (n_TOF Collaboration), Phys. Rev. C **85**, 064601 (2012).
[49] J. L. Tain, F. Gunsing, D. Cano-Ott *et al.*, J. Nucl. Sci. Technol., Supplement **2**, 689 (2002).
[50] A. Borella, G. Aerts, F. Gunsing, M. Moxon, P. Schillebeeckx, and R. Wynants, Nucl. Instrum. Methods Phys. Res., Sect. A **577**, 626 (2007).
[51] N. M. Larson, *Updated Users' Guide for SAMMY: Multi-level R-matrix Fits to Neutron Data using Bayes' Equations*, Report No. ORNL/TM-9179/R8 (Oak Ridge National Laboratory, Oak Ridge, 2008).
[52] M. Barbagallo *et al.*, Eur. Phys. J. A **49**, 156 (2013).
[53] L. M. Bollinger and G. E. Thomas, Phys. Rev. **171**, 1293 (1968).
[54] F. Gunsing, A. Leprêtre, C. Mounier, C. Raepsaet, A. Brusegan, and E. Macavero, Phys. Rev. C **61**, 054608 (2000).
[55] M. Gyulassy, R. J. Howerton, and S. T. Perkins, Report No., Vol. 11, Tech. Rep., 1972.
[56] S. F. Mughabghab, *Atlas of Neutron Resonances and Thermal Cross Sections. Resonance Parameters and Thermal Cross Sections. Z = 1-100* (Elsevier, New York, 2006).
[57] F. H. Fröhner, *SESH, computer code GA-8380* (Gulf General Atomic, San Diego,1968).